Two-Dimensional Turbulence

Guido Boffetta[1] and Robert E. Ecke[2]

[1]Department of General Physics and INFN, University of Torino, 10125 Torino, Italy; email: boffetta@to.infn.it

[2]Center for Nonlinear Studies, Los Alamos National Laboratory, Los Alamos, New Mexico 87545; email: ecke@lanl.gov

Annu. Rev. Fluid Mech. 2012. 44:427–51

First published online as a Review in Advance on October 25, 2011

The *Annual Review of Fluid Mechanics* is online at fluid.annualreviews.org

This article's doi: 10.1146/annurev-fluid-120710-101240

0066-4189/12/0115-0427$20.00

Keywords

friction drag, palinstrophy, energy flux, enstrophy flux, conformal invariance

Abstract

In physical systems, a reduction in dimensionality often leads to exciting new phenomena. Here we discuss the novel effects arising from the consideration of fluid turbulence confined to two spatial dimensions. The additional conservation constraint on squared vorticity relative to three-dimensional (3D) turbulence leads to the dual-cascade scenario of Kraichnan and Batchelor with an inverse energy cascade to larger scales and a direct enstrophy cascade to smaller scales. Specific theoretical predictions of spectra, structure functions, probability distributions, and mechanisms are presented, and major experimental and numerical comparisons are reviewed. The introduction of 3D perturbations does not destroy the main features of the cascade picture, implying that 2D turbulence phenomenology establishes the general picture of turbulent fluid flows when one spatial direction is heavily constrained by geometry or by applied body forces. Such flows are common in geophysical and planetary contexts, are beautiful to observe, and reflect the impact of dimensionality on fluid turbulence.

1. INTRODUCTION

Turbulence is ubiquitous in nature: We observe its manifestation at all scales, from a cup of coffee being stirred to galaxy formation. Among its numerous manifestations, two-dimensional (2D) turbulence is special in many respects. Strictly speaking, it is never realized in nature or in the laboratory, both of which have some degree of three-dimensionality. Nevertheless, many aspects of idealized 2D turbulence appear to be relevant for physical systems. For example, large-scale motions in the atmosphere and oceans are described, to first approximation, as 2D turbulent fluids owing to the large aspect ratio (the ratio of lateral to vertical length scales) of these systems. Charney (1971) showed that a prominent feature of 2D turbulence is present in the theory of geostrophic turbulence. **Figure 1**, showing data from a numerical simulation, a laboratory experiment, and geophysical circumstances, illustrates the similar vortex filament nature of 2D turbulence as measured in greatly disparate systems. From a theoretical perspective, 2D turbulence is not simply a reduced dimensional version of 3D turbulence because a completely different phenomenology arises from new conservation laws in two dimensions. Furthermore, the 2D Navier-Stokes equations are a simplified framework for certain turbulence problems (e.g., turbulent dispersion) because one can achieve numerically much higher spatial and temporal resolution than for a comparable simulation in three dimensions and because complications present in 3D flows such as intermittency can be avoided. When such 2D simplifications are used, it is crucial to understand how new conservation laws limit the applicability of the results.

This review is devoted to the statistics of stationary, forced-dissipated, 2D turbulence in homogeneous, isotropic conditions. We first introduce the theory and phenomenology of 2D turbulence with an eye toward the realization of these ideas in numerical simulations and in physical experiments. Next we describe how simulations and experiments are formulated to test important aspects of the theory and phenomenology. We review the critical results and their implications before ending with a summary of firm conclusions and important outstanding questions. Many interesting issues related to 2D flows are not considered, including coherent vortex formation and statistics of vortices in decaying turbulence, dynamical system approaches such as Lagrangian coherent structures and stretching fields, Lagrangian turbulence statistics, comprehensive experimental detail, and inhomogeneous flows. The effects of boundaries, stratification, rotation, and other issues related to real situations are largely excluded, except for a brief discussion with respect to experimental realizations of 2D turbulence. The interested reader should consult other reviews for details and historical perspectives (e.g., Kraichnan & Montgomery 1980, Kellay & Goldburg 2002, Tabeling 2002, van Heijst & Clercx 2009).

2. EQUATION OF MOTION AND STATISTICAL OBJECTS

We consider 2D turbulence described by the Navier-Stokes equations for an incompressible flow $\mathbf{u}(\mathbf{x}, t) = [u(x, y), v(x, y)]$:

$$\partial_t \mathbf{u} + \mathbf{u} \cdot \nabla \mathbf{u} = -(1/\rho)\nabla p + \nu \nabla^2 \mathbf{u} - \alpha \mathbf{u} + \mathbf{f}_u, \tag{1}$$

where $\mathbf{f}_u$ is a forcing term, and the term proportional to α is a linear frictional damping. Physically, friction results from the 3D world in which the flow is embedded (Sommeria 1986, Salmon 1998, Rivera & Wu 2000) and removes energy at large scales, thereby making the inverse energy cascade stationary.

Because density is constant, we take $\rho = 1$ and automatically satisfy the incompressibility condition, $\nabla \cdot \mathbf{u} = 0$, by introducing the stream function $\psi(\mathbf{x}, t)$ such that $\mathbf{u} = (\partial_y \psi, -\partial_x \psi)$.

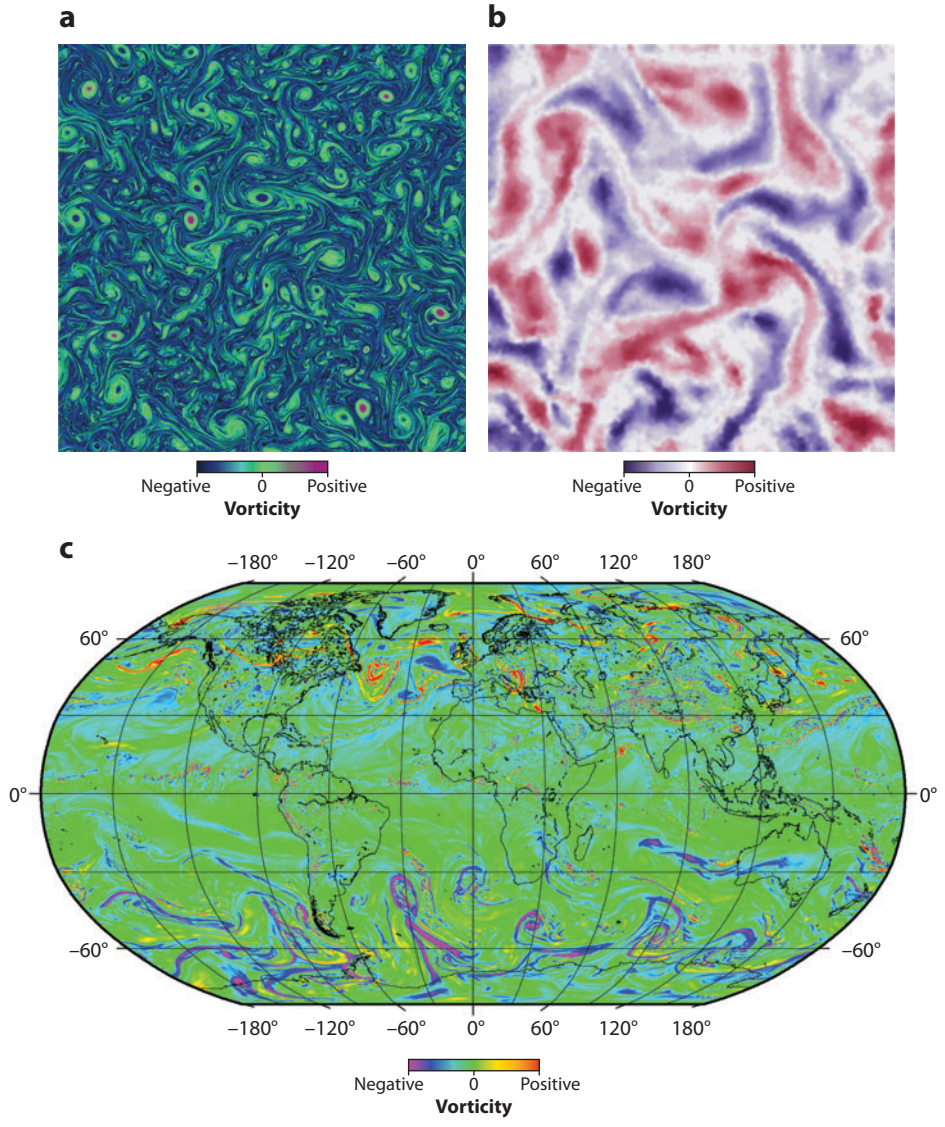

Figure 1

(*a*) Snapshot of a vorticity field in a high-resolution numerical simulation of the 2D Navier-Stokes equations. (*b*) The vorticity field of a flowing soap film. (*c*) Snapshot of a potential vorticity field from a global circulation forecast model at a layer at 200 hPa.

Equation 1 is then rewritten for the scalar vorticity field $\omega = \nabla \times \mathbf{u} = -\nabla^2 \psi$ as

$$\partial_t \omega + J(\omega, \psi) = \nu \nabla^2 \omega - \alpha \omega + f, \tag{2}$$

where $J(\omega, \psi) = \partial_x \omega \partial_y \psi - \partial_y \omega \partial_x \psi = \mathbf{u} \cdot \nabla \omega$ and $f = \nabla \times \mathbf{f}_u$. The equations of motion (Equations 1 and 2) are complemented by appropriate boundary conditions, which we take to be periodic on a square domain of size L^2 for a discussion of theoretical and numerical results; realistic boundary conditions for physical systems are discussed for experiments as appropriate.

In the inviscid, unforced limit, Equation 2 has kinetic energy $E = (1/2)\langle u^2 \rangle = (1/2)\langle \psi\omega \rangle = (1/2)\sum_{\mathbf{k}} |\hat{\omega}(\mathbf{k})|^2/k^2$ and enstrophy $\Omega = (1/2)\langle \omega^2 \rangle = (1/2)\sum_{\mathbf{k}} |\hat{\omega}(\mathbf{k})|^2$ as quadratic invariants, where $\hat{\omega}(\mathbf{k}, t) = \langle \omega(\mathbf{x}, t) e^{i\mathbf{k}\cdot\mathbf{x}} \rangle$ is the Fourier transform and $\langle \ldots \rangle$ represents a spatial average.

Turbulence is described by at least two-point statistical objects. The most commonly studied objects are the isotropic energy spectrum

$$E(k) = \pi k \langle |\mathbf{u}(\mathbf{k})|^2 \rangle \tag{3}$$

(where the average now is over all $|\mathbf{k}| = k$), from which $E = \int E(k)dk$ and $\Omega = \int k^2 E(k)dk$, and the velocity structure functions

$$S_n(r) = \langle |\delta \mathbf{u}(\mathbf{r})|^n \rangle \equiv \langle |\mathbf{u}(\mathbf{x} + \mathbf{r}) - \mathbf{u}(\mathbf{x})|^n \rangle, \tag{4}$$

where $\mathbf{r}$ is a vector separating two points in the flow. One can separate the structure function into longitudinal and transverse contributions $S_n(r) = S_n^{(L)}(r) + S_n^{(T)}(r)$ obtained from the velocity component parallel and perpendicular to $\mathbf{r}$, respectively.

Real physical flows have finite viscosity, so one needs to consider the dissipation of energy as the viscosity becomes small. For the case of zero friction ($\alpha = 0$) and no external forcing ($f = 0$), finite viscosity $\nu \neq 0$ results in the dissipation of E and Ω given by

$$\frac{dE}{dt} = -2\nu\Omega \equiv -\varepsilon_\nu(t), \tag{5}$$

$$\frac{d\Omega}{dt} = -2\nu P \equiv -\eta_\nu(t), \tag{6}$$

where we have introduced the palinstrophy $P \equiv \int dk k^4 E(k)$. Because Equation 6 bounds enstrophy from above, Equation 5 implies that $\varepsilon_\nu \to 0$ as $\nu \to 0$. This is the main difference with respect to 3D turbulence in which Ω can be amplified by vortex stretching (i.e., Equation 6 has a source term), resulting in finite energy dissipation in the limit of vanishing viscosity. In fully developed 2D turbulence, energy is not dissipated by viscosity and is dynamically transferred to large scales by the inverse cascade. As opposed to vorticity, vorticity gradients (i.e., palinstrophy) are not bounded in two dimensions, and one expects a direct cascade of enstrophy.

When dissipation is present, external forcing f is necessary to produce a statistically stationary state characterized by the injection of turbulent fluctuations at a scale ℓ_f and the removal of those fluctuations, either at much larger scales $\ell_\alpha \gg \ell_f$ by friction or at much smaller scales $\ell_\nu \ll \ell_f$ by viscosity. The two intervals of scales $\ell_f \ll \ell \ll \ell_\alpha$ and $\ell_\nu \ll \ell \ll \ell_f$ are the inertial ranges over which universal statistics are expected.

The understanding of the direction of the two cascades in the inertial ranges dates back to Fjortoft (1953). A more quantitative approach was proposed by Kraichnan (see Kraichnan 1967 and Eyink 1996). The energy and the enstrophy dissipated by friction at large scales, ε_α and η_α, respectively, are balanced by energy/enstrophy input and by viscous dissipation, i.e., $\varepsilon_I = \varepsilon_\alpha + \varepsilon_\nu$ and $\eta_I = \eta_\alpha + \eta_\nu$. The two scales characteristic of friction and viscosity are $\ell_\alpha^2 \equiv \varepsilon_\alpha/\eta_\alpha$ and $\ell_\nu^2 \equiv \varepsilon_\nu/\eta_\nu$. With the relation at the forcing scale, $\ell_f^2 \simeq \varepsilon_I/\eta_I$, one obtains

$$\frac{\varepsilon_\nu}{\varepsilon_\alpha} = \left(\frac{\ell_\nu}{\ell_f}\right)^2 \left(\frac{\ell_f}{\ell_\alpha}\right)^2 \frac{(\ell_\alpha/\ell_f)^2 - 1}{1 - (\ell_\nu/\ell_f)^2}, \tag{7}$$

$$\frac{\eta_\nu}{\eta_\alpha} = \frac{(\ell_\alpha/\ell_f)^2 - 1}{1 - (\ell_\nu/\ell_f)^2}. \tag{8}$$

In the limit of an extended direct inertial range, $\ell_\nu \ll \ell_f$, one has from Equation 7 $\varepsilon_\nu/\varepsilon_\alpha \to 0$; i.e., all the energy flows to large scales in an inverse energy cascade. Moreover, if $\ell_\alpha \gg \ell_f$, one obtains

$\eta_\alpha/\eta_\nu \to 0$; i.e., all the enstrophy goes to small scales to generate the direct enstrophy cascade. This analysis establishes the direction of energy and enstrophy cascades but does not reveal how the characteristic scales ℓ_ν and ℓ_α depend on the physical parameters α and ν.

To gain further insight about these relationships, it is convenient to move to Fourier space. Energy at a given wave number k changes at the rate

$$\frac{\partial E(k)}{\partial t} \equiv T(k) + F(k) - \nu k^2 E(k) - \alpha E(k), \tag{9}$$

where $T(k)$ represents the rate of energy transfer owing to nonlinear interactions (see Kraichnan & Montgomery 1980), whereas the other terms represent the forcing and dissipation of $E(k)$. Similarly, the nonlinear transfer of enstrophy is given by $k^2 T(k)$. The transfer of energy and enstrophy across a scale k defines the fluxes

$$\Pi_E(k) \equiv \int_k^\infty T(k')dk', \tag{10}$$

$$Z_\Omega(k) \equiv \int_k^\infty k'^2 T(k')dk', \tag{11}$$

with $\Pi_E(0) = Z_\Omega(0) = 0$ as a consequence of the conservation laws.

In the inverse-cascade range of wave numbers, $k \ll k_f$ (where $k_f \simeq 1/\ell_f$), if the energy spectrum is dominated by infrared (IR) (small-k) contributions, one has $\Pi_E(k) \sim \lambda_k k E(k)$, where λ_k is the characteristic frequency of the distortion of eddies at scale $1/k$. Dimensionally, one has $\lambda_k^2 \sim \int_{k_{min}}^k E(p)p^2 dp$, where $k_{min} \sim 1/L$ is the lowest turbulent wave number, and the upper limit in the integral reflects that scales much smaller than $1/k$ add incoherently and therefore average out on scales $1/k$.

For a scale-free solution $E(k) \sim k^{-\beta}$, the only expression that gives a scale-independent energy flux $\Pi_E(k) = \varepsilon_\alpha$ is the Kolmogorov solution:

$$E(k) = C\varepsilon_\alpha^{2/3} k^{-5/3}, \tag{12}$$

where C is the dimensionless Kolmogorov constant. Friction induces an IR cutoff at the characteristic friction scale $k_\alpha^{-1} = \ell_\alpha \simeq \varepsilon_\alpha^{1/2}\alpha^{-3/2} \simeq u_{rms}/\alpha$, and Equation 12 is expected to hold in the range $k_\alpha \ll k \ll k_f$. The extent of this inertial range of scales can be expressed in terms of an outer-scale Reynolds number that balances inertial and frictional dissipation $\mathrm{Re}_\alpha = u_{rms}/(\ell_f\alpha) = \ell_\alpha/\ell_f = k_f/k_\alpha$. The characteristic frequencies in the inverse cascade follow the scaling law $\lambda_k \simeq \varepsilon_\alpha^{1/3} k^{2/3}$; therefore, the major contribution to λ_k^2 is from $p \sim k$, consistent with the locality assumption.

For the direct-cascade range at wave numbers $k \gg k_f$, the enstrophy flux is estimated to be $Z_\Omega(k) \sim \lambda_k k^3 E(k)$. A constant enstrophy flux $Z_\Omega(k) = \eta_\nu$ gives

$$E(k) = C'\eta_\nu^{2/3} k^{-3}, \tag{13}$$

where C' is another dimensionless constant. Viscous dissipation sets the ultraviolet (large-k) cutoff at a spatial scale $k_\nu^{-1} = \ell_\nu \simeq \nu^{1/2}\eta_\nu^{-1/6}$ with a corresponding Reynolds number $\mathrm{Re}_\nu \equiv u_f \ell_f/\nu \simeq (\ell_f/\ell_\nu)^2$. The argument for the direct cascade is, however, not fully consistent. By substituting Equation 13 into the expression for λ_k^2, one obtains $\lambda_k \sim \ln(k/k_{min})$ and thereby a log-k-dependent enstrophy flux. In other words, the assumption of a scale-independent flux is not compatible with a pure power-law energy spectrum. A correction to the above argument that restores a constant $Z_\Omega(k)$ was proposed by Kraichnan (1971). By looking for a log-corrected spectrum $E(k) \sim k^{-3}[\ln(k/k_{min})]^{-n}$, he found that a constant enstrophy flux requires $n = 1/3$ and gives the prediction

$$E(k) = C'\eta^{2/3} k^{-3}[\ln(k/k_{min})]^{-1/3}. \tag{14}$$

This correction has a weak point in the assumption of locality. In the expression in Equation 14, λ_k^2 is IR dominated by wave numbers $p \ll k$. Therefore, the situation is quite different from a Kolmogorov $-5/3$ spectrum (in both two and three dimensions) in which transfer rates are local in k. Rather, it is similar to the stirring of a passive scalar in the Batchelor regime (Batchelor 1959) in which the dominant straining comes from the largest scales. The analogy with passive scalars becomes stronger in the presence of friction: The inclusion of a damping term in Equation 1 has a dramatic effect on the direct enstrophy cascade in which it changes the exponent of the spectrum, as discussed in Section 4.3.

For an energy spectrum of the form $E(k) \sim k^{-\beta}$, one expects power-law scaling in r for the second-order velocity structure function. Indeed, for any λ, we have $S_2(\lambda r) = 4\int_0^\infty dkE(k)[1 - J_0(k\lambda r)] = \lambda^{\beta-1}S_2(r)$, which implies $S_2(r) \sim r^{\beta-1}$. This argument is consistent only if the integral over k is not IR or ultraviolet divergent (i.e., is dominated by local contributions). Taking into account the asymptotic behaviors of $J_0(x)$, one obtains the so-called locality condition for convergence: $1 < \beta < 3$. Under this condition, $E(k)$ and $S_2(r)$ contain the same scaling information. In the case of the inverse cascade, the prediction is therefore $S_2^{(L)}(r) = C_2\varepsilon^{2/3}r^{2/3}$, with $C_2 = \sqrt{3}\pi/[2^{5/3}\Gamma^2(4/3)]C \approx 2.15C$. For the direct cascade, Equation 13 gives $S_2(r) \sim r^2$, but this is at the border of the IR locality condition ($\beta = 3$). Therefore, the velocity structure functions are dominated by the largest scales and are not informative about the small-scale turbulent components (the same r^2 behavior is expected for any spectrum with $\beta > 3$). More information is obtained by looking at the statistics of small-scale-dominated quantities, the most natural being structure functions of vorticity.

Constant energy and enstrophy fluxes in the respective inertial ranges imply exact relations for the third-order structure function (see Frisch 1995, Bernard 1999, Lindborg 1999, Yakhot 1999). For homogeneous, isotropic conditions over the range of scales in the inverse cascade ($r \gg \ell_f$), one has

$$S_3^{(L)}(r) \equiv \langle[\delta u_\parallel(r)]^3\rangle = 3\langle\delta u_\parallel(r)[\delta u_\perp(r)]^2\rangle = \frac{3}{2}\varepsilon_I r, \tag{15}$$

which is the 2D equivalent of the 3D Kolmogorov 4/5 law. In the range of scales of the direct enstrophy cascade ($r \ll \ell_f$), the prediction is

$$S_3^{(L)}(r) = \frac{1}{8}\eta_I r^3, \tag{16}$$

which can also be written for the mixed velocity-vorticity structure function, representing the enstrophy flux, as

$$\langle\delta u_\parallel(r)[\delta\omega(r)]^2\rangle = -2\eta_I r. \tag{17}$$

Assuming self-similarity, Equation 15 leads to the scaling exponent of 1/3 for velocity fluctuations in the inverse cascade and therefore to a Kolmogorov prediction for the exponents of the velocity structure functions $S_n(r) \sim r^{\zeta_n}$ with $\zeta_n = n/3$. At variance with the 3D case in which deviations are found (Frisch 1995), this mean field prediction is supported by simulations and experiments in the inverse cascade of 2D turbulence.

3. METHODS AND APPROACHES

In this section, we discuss general methods and approaches for experimental realizations and numerical simulations of 2D turbulence. Physical fluid systems are intrinsically 3D. By constraining motion in one spatial direction, however, one can produce fluid motion that is approximately 2D. There are numerous ways to apply such a constraint with quite different resultant 3D perturbations. There are two main types of constraints: (*a*) body forces including stratification, rotation,

and magnetic fields and (*b*) geometric anisotropy in which the length scale in one direction is much smaller than in the other two. Both constraints are important in geophysical and astrophysical systems. For example, one can treat some aspects of motion in atmospheres or oceans as approximately 2D because of the much smaller depth of the atmosphere (ocean), ~10 km, relative to lateral global scales, 10^3–10^4 km.

We focus here on two experimental realizations of 2D turbulence that have been widely utilized, namely thin electrically conducting layers driven by a combination of a fixed array of magnets with an applied electrical current and soap films flowing under the force of gravity. We do not discuss other realizations of 2D turbulence using rotation, stratification, and magnet fields. In all laboratory realizations of 2D turbulence, the flows are damped by coupling to boundaries. We treat this as a linear frictional damping proportional to the velocity with coefficient α as in Equation 1 with a form discussed below for each system. A nondimensional measure of damping, $\alpha' = \alpha/\omega_{rms}$ (or, equivalently, a Reynolds number $\mathrm{Re}_{\alpha'} = 1/\alpha'$), allows one to compare the relative importance of friction among different systems. In the cases considered here, the fluid equations governing the quasi-2D flows have not been unambiguously demonstrated to satisfy the 2D Navier-Stokes equation (see Couder et al. 1989, Paret et al. 1997, Chomaz 2001, Rivera & Wu 2002), but the mapping is not an unreasonable one. Our main focus here is on experiments in which one can measure the full velocity field and thereby extract information that elucidates the physics of 2D turbulence in a complete way. An important point for experiments is that the degree to which the results for idealized 2D turbulence apply to the quasi-2D systems is a measure of the applicability of these predictions to 3D systems such as Earth or planetary atmospheres.

As opposed to laboratory experiments, truly 2D flows are easily realizable in silico; therefore, direct numerical simulation (DNS) is one of the most powerful methods for studying 2D turbulence (see **Figure 1**). Lilly (1969) first attempted the simulation of 2D turbulence using a finite-difference scheme on a 64×64 grid to study both the cascades predicted by Kraichnan. This early attempt was not successful in observing coexisting cascades as much higher resolution is actually needed (Boffetta 2007).

Many simulations of 2D turbulence do not integrate Equation 2 but instead consider a variant in which viscous dissipation and friction are replaced by higher-order terms $(-1)^{p+1}\nu_p\nabla^{2p}\omega$ and $(-1)^{q+1}\alpha_q\nabla^{-2q}\omega$, respectively. The motivation for the use of hyperviscosity ($p > 1$) and hypofriction ($q > 0$) is to reduce the range of scales over which dissipative terms contribute substantially, thereby extending the inertial range for a given spatial resolution. Recent studies (Lamorgese et al. 2005, Frisch et al. 2008, Bos & Bertoglio 2009) suggest that these modified dissipation approaches can seriously affect the statistics at the transition between inertial and dissipative scales.

Energy and enstrophy input for DNS are usually implemented numerically using a Gaussian stochastic forcing with zero mean and correlation function $\langle f(\mathbf{x}', t')f(\mathbf{x}, t)\rangle = F(\mathbf{x}'-\mathbf{x}, t'-t)$. The spatial dependence of F is chosen to restrict the injection to a range of scales around ℓ_f, whereas the temporal component is usually white noise, $F(\mathbf{x}'-\mathbf{x}, t'-t) = F(r)\delta(t-t')$, which fixes a priori the mean enstrophy (and energy) input as $\eta_I = F(0)/2$ (Novikov 1965).

Experiments on 2D turbulence have external forcing that is fixed in space, either by a grid, as in decaying turbulence in a soap film channel, or by the fixed array of magnets for horizontal soap films and stratified layers. Standard magnet configurations include (*a*) a pseudo-random set of positions with a mean separation distance (Williams et al. 1997, Voth et al. 2003, Twardos et al. 2008), (*b*) block random forcing in which small magnets of the same polarity are arranged in larger blocks (Paret et al. 1999, Boffetta et al. 2005) in an attempt to produce a random large-scale forcing (this scheme results in energy injection at the scale of the magnet as well as at the block scale), (*c*) Kolmogorov flow using strip magnets (Rivera & Wu 2000) or lines of magnets in which case there is a weak perturbation on pure parallel shear flow, and (*d*) square-array forcing.

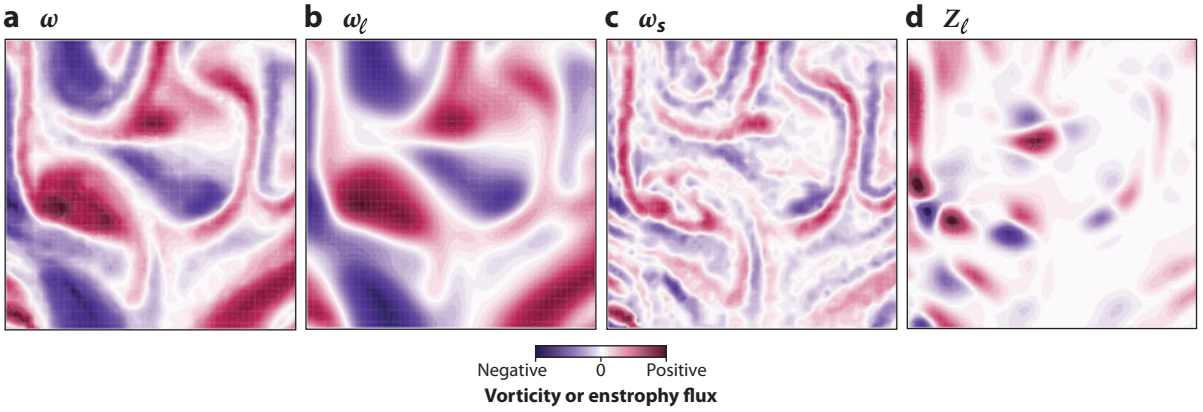

Figure 2

The decomposition of a soap-film vorticity field using the filter approach to obtain the enstrophy flux: (*a*) unfiltered vorticity ω, (*b*) filtered large-scale vorticity ω_ℓ, (*c*) small-scale vorticity $\omega_s = \omega - \omega_\ell$, and (*d*) enstrophy flux Z_ℓ.

Experimentally, one has more options for temporal forcing. The electric current can be sinusoidally periodic or square-wave periodic or it can be telegraph noise, i.e., with constant amplitude but varying intervals of positive and negative polarity of the current with zero mean. The optimal temporal forcing is not well understood, but some general observations can be noted: If the frequency is too high, the forcing does not couple well with the fluid degrees of freedom, and little net energy is injected into the fluid. The optimal transfer of energy occurs for direct-current forcing, but there is preferential buildup at the injection scale and possible coupling to large-scale inhomogeneities in the forcing (e.g., magnet arrangement, layer height). A systematic study of forcing has not been performed for experimental 2D turbulence.

An analysis method that has proved useful for both experimental (Rivera et al. 2003, Chen et al. 2006) and numerical (Xiao et al. 2009) data is based on the filter approach, the basis for large-eddy simulations. This methodology can be applied either to the velocity field to yield information about the energy flux or to the vorticity field to obtain the enstrophy flux. We consider the vorticity here for simplicity, with details found elsewhere (Xiao et al. 2009). The vorticity field $\omega(x, y)$ is smoothed with a low-pass filter with cutoff ℓ, e.g., $G_\ell(r) \sim e^{-r^2/(2\ell^2)}$, to create a filtered vorticity field $\bar{\omega}_\ell$. One obtains an equation for the large-scale enstrophy Ω_ℓ:

$$\partial_t \Omega_\ell(\mathbf{r}, t) + \nabla \cdot \mathbf{K}_\ell(\mathbf{r}, t) = -Z_\ell(\mathbf{r}, t), \tag{18}$$

where $\mathbf{K}_\ell$ is the space transport of enstrophy, $Z_\ell(\mathbf{r}, t) = -\nabla\bar{\omega}_\ell(\mathbf{r}, t)\cdot\sigma_\ell(\mathbf{r}, t)$ is the enstrophy flux out of large scales greater than ℓ into small-scale modes, and $\sigma_\ell = \overline{(u\omega)}_\ell - \bar{u}_\ell\bar{\omega}_\ell$ is the space transport of vorticity owing to the eliminated small-scale turbulence. The exciting aspect of this filter method is that one obtains scale-to-scale information as a function of real space coordinates. An example of the filter approach drawn from experimental soap-film data (Rivera et al. 2003) is shown in **Figure 2** in which the vorticity field ω is decomposed into the filtered large-scale field $\bar{\omega}_\ell$ and the small-scale field $\bar{\omega}_s = \omega - \bar{\omega}_\ell$. The resultant Z_ℓ shows the physical space distribution of enstrophy flux. This representation provides an opportunity to quantitatively test physical mechanisms of the direct enstrophy process (Rivera et al. 2003) or the inverse energy cascade using the filtered energy flux Π_ℓ (Chen et al. 2006, Xiao et al. 2009).

3.1. Electromagnetically Forced Conducting Fluid Layers

An effective way to induce fluid motion in a highly controlled manner in thin layers of conducting fluids is to arrange an array of magnets beneath the layer and to apply a spatially uniform current in the plane of that layer. The resulting Lorentz force induces horizontal motion. A schematic illustration of an electromagnetic layer (EML) experiment is shown in **Figure 3*a***. The flexibility of the placement of the magnets and of the application of different time sequences of the electric current makes this system amenable to experimental study. In particular, there is no mean flow, and because of the strong two-dimensionality of the flow, particles are straightforward to track directly, and velocity fields are obtained using particle tracking velocimetry (PTV) [or, with less fidelity, particle image velocimetry (PIV)]. Examples of such reconstructions are shown in **Figure 3*b*,*c***. An advantage of EML systems is approximately incompressible Newtonian fluid flow for modest forcing with well-understood and controllable boundary drag, which makes them suitable for studies of the inverse energy cascade and for Lagrangian measurements. However, the Reynolds numbers of the flow are limited because vigorous forcing induces compressibility effects (or thickness variations for soap films), including surface waves, and may cause Joule heating of the layers at higher currents. Finally, the relatively large thickness of salt layers makes the direct cascade hard to resolve as the generation of fine vortex filaments is limited by the layer thickness.

There have been several manifestations of EML systems using different fluids and magnetic configurations: a layer of mercury over an array of source/sinks of electric current with a large-scale, constant magnetic field; a layer of saltwater with and without buffering layers to reduce bottom drag; and a soap film made electrically conducting by the addition of salt. For each system we describe the typical ranges of parameters, including drag coefficients and Reynolds numbers.

One of the first experiments on 2D turbulence was done by Sommeria (1986) in a $h = 2$-cm-deep layer of mercury with lateral dimensions $L = 12$ cm and aspect ratio $\Gamma = L/h = 6$. A constant field magnet (0.1–1 Tesla) generated a Hartmann layer δ_H between 30 and 250 μm. A square array of alternating sources of electric current induced vorticity on a forcing scale $\ell_f \approx 1$ cm. Electric potential probes measured the local velocity with high accuracy. Owing to the small kinematic viscosity of mercury, $\nu \approx 10^{-3}$ cm^2 s^{-1}, the injection-scale Reynolds number $\mathrm{Re}_\nu = u_{rms}\ell_f/\nu$

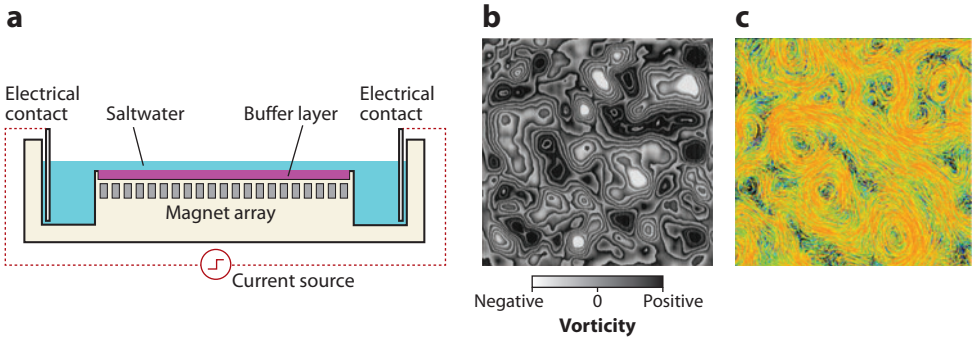

Figure 3

(*a*) Schematic illustration of an electromagnetically forced thin layer system with an immiscible nonconducting bottom fluid and an upper salt solution. Differences in the apparatus depend on experimental details, e.g., mercury with a thin Hartmann layer (Sommeria 1986) or a miscible bottom salt solution with a pure-water upper layer (Paret & Tabeling 1997). Examples of 2D field measurements in electromagnetic layers include (*b*) a vorticity field in a stationary inverse cascade by Paret & Tabeling (1997) and (*c*) particle trajectories of a velocity field for stratified immiscible layers described by Rivera & Ecke (2005) (false color). Panel *b* reproduced by permission, copyright © 1997 by the American Physical Society.

reached 10^4, whereas the outer-scale Reynolds number $\mathrm{Re}_\alpha = u_{rms}/(\ell_f \alpha)$ was set by frictional damping so that $\mathrm{Re}_\alpha < 5$. Similarly, $1 < \alpha' < 10$, reflecting the large damping of the thin Hartmann layer.

The most widely studied system for 2D turbulence is a single saltwater layer with thickness $0.2 < h < 1$ cm and $L \sim 20$ cm (Cardoso et al. 1994, Bondarenko et al. 2002) or two layers of fluid, either miscible (Marteau et al. 1995) or immiscible (Rivera & Ecke 2005) combinations, with similar thicknesses. The aspect ratio $\Gamma = L/h \sim 100$ is considerable although $L/\ell_f \sim 20$ for $\ell_f = 1$ cm. Boundary drag is an important feature of this system and is relatively easy to calculate. For a single layer, the rigid boundary condition on the bottom and free-surface boundary at the top imply $\alpha = \nu\pi^2/(2h^2)$ (Dolzhanskii et al. 1992). With typical values of $h = 0.3$ cm and $\nu = 0.01$ cm^2 s^{-1}, one obtains $\alpha \approx 0.5$ s^{-1}. Using the miscible double-layer configuration—top water layer over bottom saltwater layer, both with height h—α is reduced by a factor of four owing to the increased mass of the layer, yielding $\alpha \approx 0.13$ s^{-1} for $h = 0.3$ cm. The disadvantage of this configuration is that the fluids can mix vertically. Another arrangement that avoids this problem is the use of saltwater over a heavier, immiscible fluid (Rivera & Ecke 2005). If one assumes a linear shear in the bottom layer, the damping coefficient is given by $\alpha = (\rho_b/\rho_t)\,[\nu_b/(hd)]$, where d is the height of the lower layer; ρ_t and ρ_b are the top and bottom fluid densities, respectively; and ν_b is the bottom fluid's kinematic viscosity. Using typical values of $h = d = 0.3$ cm, $\rho_t \approx \rho_b$, and $\nu_b = 0.01$ cm^2 s^{-1}, one obtains $\alpha = 0.12$ s^{-1}, similar to the miscible, two-layer system. Because the saltwater layer is the bottom layer in the miscible case and the top layer in the immiscible case, driving is more effective for the former because the magnetic field falls off with distance. In terms of forcing combined with frictional damping, the limit of Re is approximately 500, with the maximum achieved $\mathrm{Re}_\alpha \approx 20$, and $\alpha' \approx 0.01$. The effective two-dimensionality of these configurations depends on the forcing, the layer depths, the ratio of depths to forcing h/ℓ_f, and the type of flow (a small number of vortices or many vortices in a turbulent state) (Paret et al. 1997, Akkermans et al. 2008, Shats et al. 2010), but there are ranges of parameters in which the two-dimensionality and incompressibility of the flow are well satisfied. The great advantage of this EML system is the ease of both construction and measurement.

The third EML system is electromagnetically forced horizontal soap films. Soap films are thinner, typically between 10 and 50 μm with Γ on the order of 3,000, but involve more complex dynamical equations (Chomaz 2001, Couder et al. 1989). Rivera & Wu (2000, 2002) suspended a relatively thick (approximately 50 μm) electrically conducting soap film in a square frame of area 7×7 cm^2 over a glass plate located a distance d below the film. Two opposite sides of the frame were metallic so that the authors could apply a voltage difference. Placed over an array of magnets, the current induced a horizontal Lorentz forcing of the flow. The viscosity of the soap film was the same order as water, $\nu \approx 0.03$ cm^2 s^{-1}, and the drag coefficient was in the range $0.4 < \alpha < 1.5$ s^{-1} depending on d (linear shear with a finite contribution of air drag from above and below the film) (Rivera & Wu 2002). Typical parameters are $\mathrm{Re} < 250$, $\mathrm{Re}_\alpha < 20$, and $\alpha' \approx 0.01$, quite similar to saltwater EML systems.

3.2. Soap-Film Channels

Thin surfactant layers (soap films) were introduced as models of 2D flows by Couder et al. (1989) and Gharib & Derango (1989). These early experiments were groundbreaking and suggestive of interesting turbulent properties, but the measurement capabilities were limited, and the films were not very stable. Gharib & Derango (1989) obtained velocity measurements using laser-Doppler velocimetry (LDV) in a horizontal flowing soap-film-channel configuration. This setup

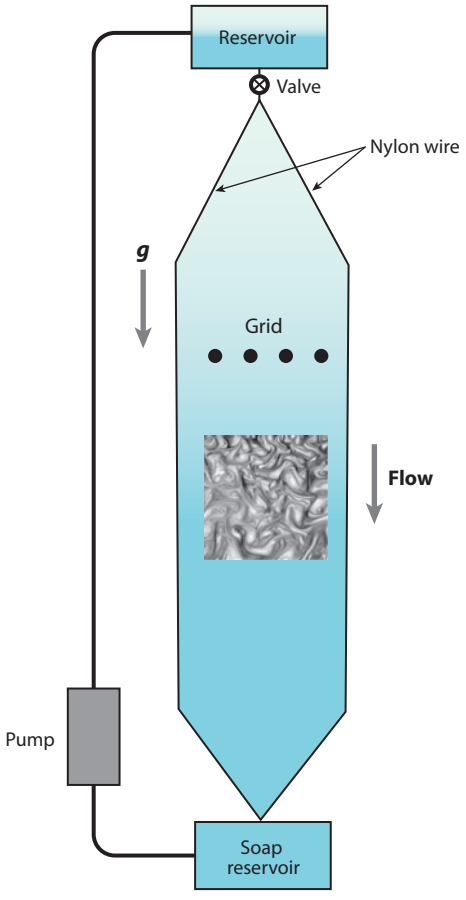

Figure 4

Schematic of a vertical soap-film channel. The film is constantly replenished using a pump, and the flow rate is adjusted with a valve from the top reservoir. The frame of the channel is typically made of nylon wires. The width of the channel can be comfortably varied in the range 1–10 cm with a total height of 100–200 cm.

resembled a 3D wind tunnel in that turbulence was created, for example, by a grid placed in the flow and subsequently decayed downstream. A variant on the horizontal soap-film channel was later developed by Kellay et al. (1995), who employed a vertical configuration (or one tilted at an angle with respect to the vertical direction as in Vorobieff et al. 1999) (see **Figure 4**). The surfactant-water solution, typically 2% of commercial detergent in water, is continuously recirculated to the top of the channel by a pump. The thin film flows between the two nylon wires at a mean velocity ranging from approximately 0.5 m s^{-1} to 4 m s^{-1} with thicknesses between 1 and 30 μm. The resultant soap film can last for several hours. Turbulent flow is generated in the film channel by a 1D grid inserted in the film (see **Figure 4**) with the separation between the teeth and their size determining the injection scale.

The first quantitative probes of fluid flow in these soap films were single-point measurements of velocity (Kellay et al. 1998, Kellay & Goldburg 2002) including LDV or optical fiber velocimetry, which allow for simple and accurate measurements of the velocity at rather high sampling rates (2,000–3,000 Hz) but are limited to a single point (or a small number of points), and the reconstruction of spatial features requires the use of the Taylor frozen-turbulence hypothesis. Rivera

et al. (1998, 2003) and Vorobieff et al. (1999) used PIV or PTV approaches to measure velocity fields in soap films with the soap seeded with particles (which are small compared to the film thickness). Although this method yields the entire velocity field, power spectra derived from the fields have less overall resolution than single-point measurements because the spatial resolution of PIV/PTV is limited to approximately 100 × 100 points or less.

The flowing system is an open one in which structures are advected with the mean flow. Thus real-time dynamics are difficult, and measurements consist of ensemble averages over interrogation areas at different downstream distances from the turbulence-generating grid. At intermediate downstream distances, on the order of the film width, the decay of energy over the interrogation region is small enough that the turbulence can be considered approximately isotropic and homogeneous. (This assumption has not been as carefully studied for 2D turbulence as it has in three dimensions.) Although not useful for the study of the inverse energy cascade because of the decaying nature of the open flow, flowing soap films are ideal for exploring the direct enstrophy cascade. The mean-flow-based Reynolds number is approximately 1,000; the Taylor Reynolds number $\mathrm{Re}_\lambda = u_{rms}\lambda/\nu \approx 100$, where $\lambda = (u_{rms}/\omega_{rms})^{1/2}$; the damping coefficient $\alpha \approx 0.1\ \mathrm{s}^{-1}$; and $\alpha' \approx 0.0002$. An estimate of α for a typical flowing soap film, assuming a Blasius laminar boundary layer and velocity fluctuations δu small compared to the mean velocity U, is $\alpha \simeq (\rho_a/(h\rho_s))(\nu_a U/y)^{1/2} \approx 0.15\ \mathrm{s}^{-1}$, where ρ_a and ρ_s are the air and soap-film densities, respectively; ν_a is the kinematic viscosity of air; and y is the downstream distance from the outlet flow nozzle.

4. NUMERICAL AND EXPERIMENTAL RESULTS

The Kraichnan-Batchelor picture of 2D turbulence lays out significant and testable predictions about spectra, structure functions, conserved fluxes, and other features of the turbulent state. We present numerical and experimental data that test the main predictions of the basic theory. Because both experiments and numerics have limited spatial range, the main results consist of tests of either the inverse cascade or the direct cascade. We then briefly consider the study of the dual-cascade picture drawn mostly for numerical simulations.

4.1. Statistics of the Inverse Cascade

The first observations of the inverse energy spectrum (Equation 12) were in DNS by Lilly (1969), Siggia & Aref (1981), Frisch & Sulem (1984), and Herring & McWilliams (1985). The first experimental study was performed by Sommeria (1986) in a mercury-layer apparatus in which he observed an inverse cascade over approximately a half-decade of wave numbers for nonstationary conditions with a Kolmogorov constant of $3 \le C \le 7$. Numerical simulations of the inverse cascade followed the evolution of computing power, providing convincing evidence of Kolmogorov scaling and more precise measurements of dimensionless constants (see **Figure 5*a***). A $k^{-5/3}$ spectrum over more than one decade (resolution 512^2) was observed by Maltrud & Vallis (1991) with $C = 6 \pm 0.5$. Using a resolution of $2{,}048^2$, Smith & Yakhot (1993) measured a similar value $C \simeq 7.0$. The statistics of velocity fluctuations $\delta u(r)$ for scales r in the inertial range were also found to yield a probability distribution function (PDF) that was close to Gaussian, indicating the absence of intermittency.

Boffetta et al. (2000) investigated intermittency and Gaussian distributions in the inverse cascade with high statistical accuracy and found that $S_n^{(L)}(r)$ for $n \le 7$ followed closely dimensional scaling, ruling out the possibility of 3D-like intermittency in the inverse cascade (**Figure 6*a***). Nevertheless, the PDF of longitudinal velocity fluctuations cannot be exactly Gaussian as a consequence of the 3/2 law (Equation 15). They found that despite the small value of the skewness

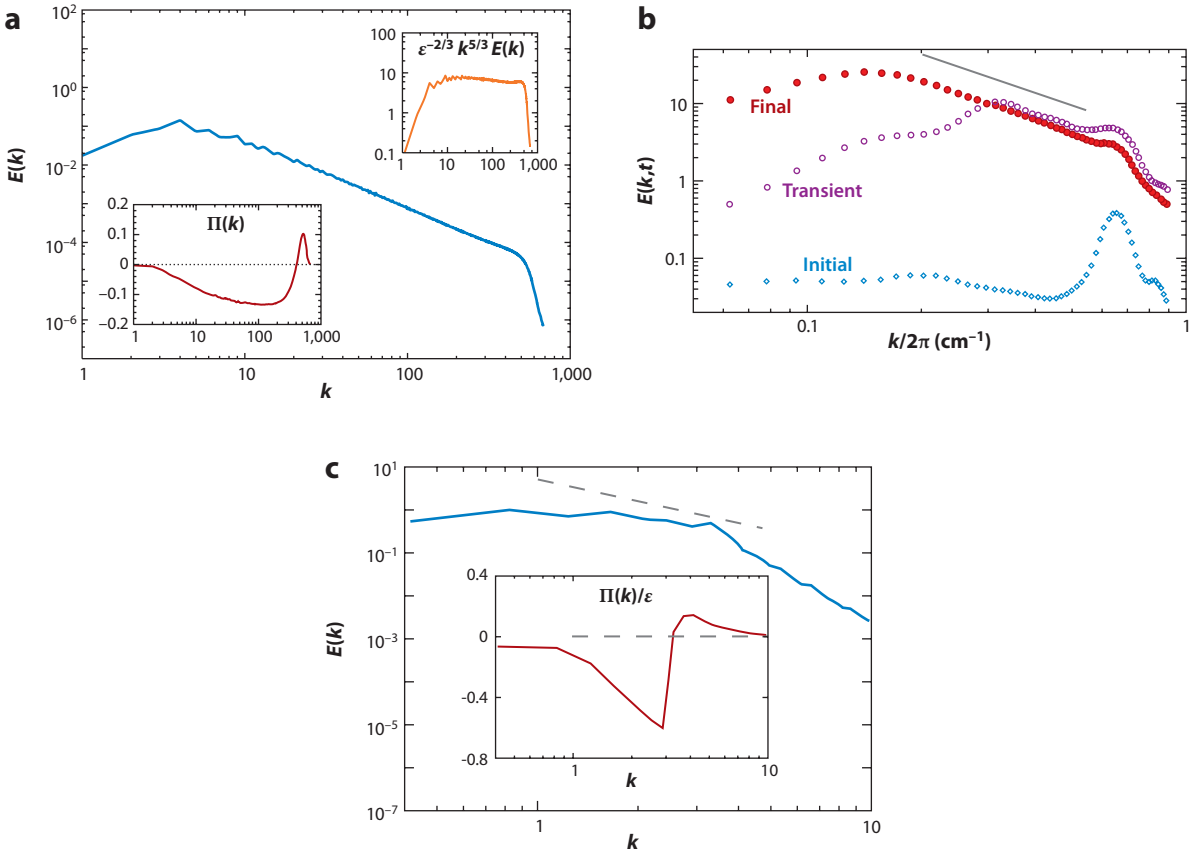

Figure 5

(*a*) $E(k)$ from a DNS of the inverse cascade at a resolution $2{,}048^2$. The forcing is at $k = 600$, and linear friction removes energy around $k = 6$. Energy flux $\Pi(k)$ is shown in the lower inset. The upper inset shows the compensated spectrum $\varepsilon^{-2/3}k^{5/3}E(k)$, which gives the Kolmogorov constant $C = 6.0 \pm 0.4$. Figure adapted from Boffetta et al. (2000), copyright (2000) by the American Physical Society. (*b*) $E(k, t)$, showing the temporal development of an inverse cascade. The solid line is the 5/3 power law. Figure reprinted with permission from Paret & Tabeling (1997), copyright (1997) by the American Physical Society. (*c*) The energy spectrum $E(k)$ and (*inset*) spectral density flux $\Pi(k)/\varepsilon$ for an inverse cascade in an electromagnetic-layer experiment. The dashed line represents Kolmogorov scaling. Figure adapted from Chen et al. (2006), copyright (2006) by the American Physical Society.

$s = S_3^{(L)}/[S_2^{(L)}]^{3/2} = (3/2)/(C_2)^{3/2} \simeq 0.03$, the PDF cannot be considered Gaussian because, for large fluctuations, the antisymmetric component of the PDF becomes important.

Recent DNS of the inverse cascade by Xiao et al. (2009) and related combined numerical-experimental comparisons by Chen et al. (2006) are consistent with these scaling results with added insight into the mechanism of the inverse cascade based on a filter-space decomposition of the velocity field and the local energy flux Π_ℓ. The theory, based on a multiscale gradient expansion developed by Eyink (2006), yields excellent predictions for numerically and experimentally obtained data (see Chen et al. 2006, figure 2). The interpretation of the mechanism is complicated by the highly nonlinear nature of the turbulent state but seems to involve coupling the large-scale stress to the thinning of smaller-scale vortices (see Chen et al. 2006 and the detailed discussion in Xiao et al. 2009, as well as argument against this interpretation in Cummins & Holloway 2010). Nevertheless, the process of vortex merger was shown by experiment (e.g., Paret & Tabeling

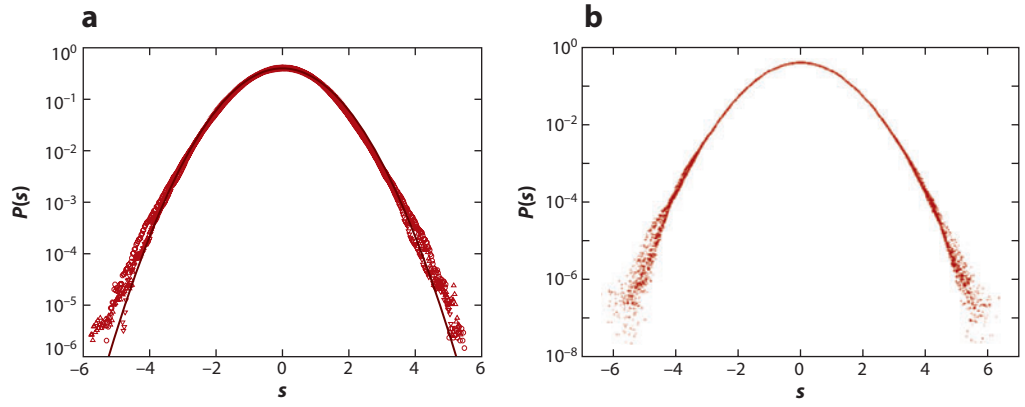

Figure 6

(*a*) Rescaled PDFs of scaled longitudinal velocity increments $s = \delta v/(\delta v^2)^{1/2}$ for different separations in the inertial range of the inverse cascade from direct numerical simulation. Panel reprinted with permission from Boffetta et al. (2000), copyright © 2000 by the American Physical Society. (*b*) Same quantity obtained from an experimental electromagnetic-layer system; panel reprinted by permission from Paret-Tabeling (1998), copyright © 1998 by the American Physical Society.

1997) and by all published DNS (with friction) to be qualitatively unimportant in that large-scale vortical structures were not observed. These observations were made quantitative by Chen et al. (2006) and Xiao et al. (2009) by demonstrating that a merger contributed little to inverse energy flux (Xiao et al. 2009).

Numerical results showing Kolmogorov-Kraichnan scaling are corroborated by a series of laboratory experiments. In a forced-EML experiment, Paret & Tabeling (1997) measured the development of an inverse cascade with a $k^{-5/3}$ spectrum in stationary conditions with a value for the Kolmogorov constant $C \simeq 6.5 \pm 1$ (**Figure 5**). For the same experiment, $S_n^{(L)}$ were shown to follow Kolmogorov scaling (Paret & Tabeling 1998), and the velocity PDFs were very close to Gaussian (**Figure 6*b***) with a skewness $s \simeq 0.05$. There are many experiments probing different aspects of the inverse energy cascade, including a careful analysis of the energy budget and spatial scales in an EML soap experiment (Rivera & Wu 2000, 2002), a description of center and hyperbolic structure distributions (Rivera et al. 2001), and Richardson dispersion in the inverse cascade (Jullien et al. 1999, Boffetta & Sokolov 2002, Rivera & Ecke 2005).

DNS by Borue (1994), Danilov & Gurarie (2001), and Bos & Bertoglio (2009) that result in a steeper slope at small k consistent with a k^{-3} scaling seem to arise from strong hypofriction dissipation at small scales, producing states that mimic the condensate picture described below. This result may arise from the hypofriction generating an abrupt drop in the spectrum that prevents the transfer of energy above the damping scale with a resultant energy pileup at that scale.

4.2. Energy Condensation at Large Scales

Kraichnan (1967) discussed the inverse cascade in a finite box in the absence of a large-scale dissipation mechanism. If boundary conditions allow for a lowest wave number $k_{min} \sim 1/L$, he conjectured that energy would eventually accumulate in this mode, leading to a condensate, analogous to a Bose-Einstein condensate, in which almost all the energy and enstrophy are concentrated around k_{min} with $\Omega \simeq k_{min}^2 E$. Although not reachable in either DNS or experiment, for finite viscosity and energy sufficiently large, a stationary state may be reached for an asymptotic value of the energy of the order $E \simeq \varepsilon/(2\nu k_{min}^2)$ (Eyink 1996).

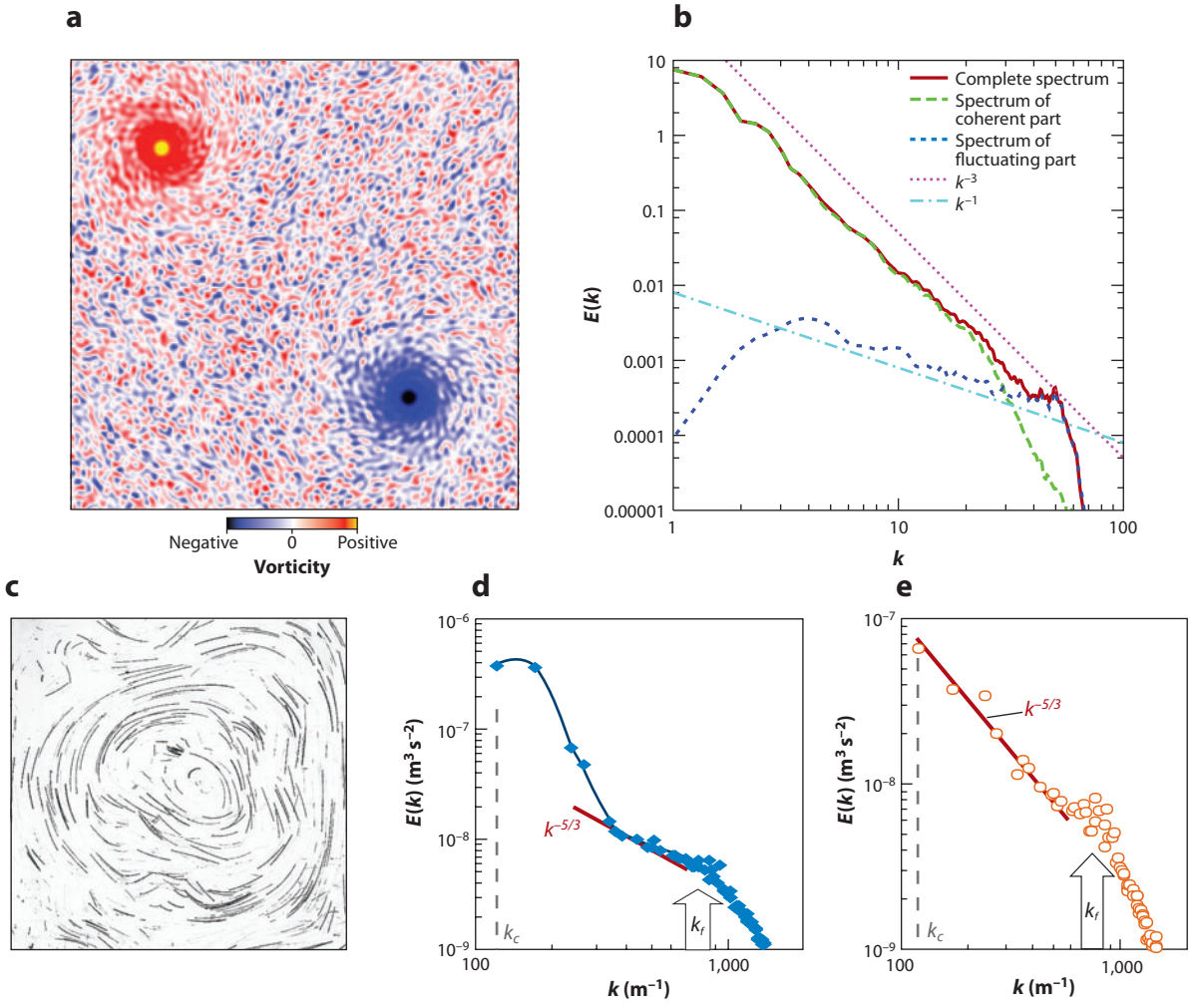

Figure 7

(*a*) Vorticity field after the formation of the condensate in numerical simulations. Two oppositely signed vortices are required by the condition of zero mean vorticity imposed by the numerical code. (*b*) Corresponding $E(k)$ showing the spectra of the complete field, the coherent part, and the fluctuating part with scalings as indicated. Panels *a* and *b* reprinted with permission from Chertkov et al. (2007), copyright © 2007 by the American Physical Society. (*c*) Trajectories of tracer particles showing the box-size vortex condensate in an electromagnetic-layer (EML) experiment. (*d*,*e*) Energy spectra for the EML experiments showing the full-field segment and spectrum with the coherent vortex subtracted, respectively, and with scalings labeled. Panels *c*–*e* reprinted with permission from Xia et al. (2011), Macmillan Publishers Ltd: *Nature Physics*, copyright © 2011.

Energy condensation was qualitatively observed in DNS by Hossain et al. (1983) and extensively studied by Smith & Yakhot (1993, 1994), who quantified the formation of a condensate peak at k_{min} with a strong departure from Gaussianity for small-scale velocity increments. In physical space, the condensation appears as the formation of two strong vortices of opposite sign.

The dynamics of the condensate was recently addressed by Chertkov et al. (2007) using DNS with $\alpha = 0$, as shown in **Figure 7*a*,*b***. The analysis separates the coherent part of the vorticity from the background to study the evolution of the condensate. The radial vorticity distribution in the condensate is described by $\Omega(r, t) = \sqrt{t}F(r/\ell_f)$, where the time dependence is based on

an energy balance argument and $F(x) \sim x^{-1.25}$. The spectrum, which strongly deviates from the Kolmogorov-Kraichnan slope, is close to the k^{-3} observed by Borue (1994). The spectrum is dominated by the coherent phase: After the decomposition, the spectrum of the background is close to k^{-1}.

The formation of the condensate was also observed in laboratory experiments. Paret & Tabeling (1998) used an EML setup with constant energy input provided by a current with constant amplitude and random sign. At late times, the flow was dominated by a single vortex near the center of the cell (at variance with DNS because of different boundary conditions). The size of the vortex core was the order of the forcing scale (see Paret & Tabeling 1998, figure 19) as observed in DNS. The experimental results were directly compared with DNS by Dubos et al. (2001) in which a strong departure from Gaussianity for longitudinal velocity increments was attributed to the large-scale vortex structures. The condensate was further investigated in an EML system by Shats et al. (2005) and Xia et al. (2008, 2011) (see **Figure 7*c–e***). In the presence of a strong condensate, the spectrum at small wave numbers becomes steep, with $E(k) \sim k^{-3}$. When the coherent vortex part is subtracted out, however, $E(k) \sim k^{-5/3}$, somewhat steeper than the k^{-1} obtained in the DNS decomposition.

4.3. Statistics of the Direct Cascade

As opposed to the inverse energy cascade, the mechanism for the direct cascade is well agreed upon, namely that large-scale vortices near the injection scale induce vortex-gradient stretching that terminates with fine vortex filaments that dissipate vorticity via viscosity. Setting aside, for the moment, the subtle issue of logarithmic corrections, we consider the energy spectrum $E(k)$. Early DNS reported results very different from theoretical expectations, with $E(k)$ much steeper than k^{-3}, both for decaying simulations by McWilliams (1984) and for forced ones by Basdevant et al. (1981) and Legras et al. (1988), in which corrections to the spectral exponent were found to depend on the forcing mechanism. These deviations appear to be correlated with the presence of strong, long-living vortices, which dominate the vorticity field, similar to decaying turbulence in which such vortices arise spontaneously (Fornberg 1977, McWilliams 1984, Bracco et al. 2000). If vortices (regions with a vorticity magnitude larger than a threshold) are removed by filtering, the remaining background field gives an energy spectrum consistent with the Kraichnan prediction k^{-3} (Benzi et al. 1986).

A less artificial way to avoid large, persistent vortices is to drive the system with a random-in-time forcing. In this case, numerical simulations by Herring & McWilliams (1985) and Maltrud & Vallis (1991) show that vortices, if present, are much weaker, and the spectrum is closer to the theoretical prediction. A set of simulations by Borue (1993) with white-in-time Gaussian forcing and for both normal and hyperviscous dissipation showed that $E(k)$ approaches k^{-3} with increased spatial resolution (see **Figure 8**). The Kolmogorov constant was estimated to be $C' = 1.6 \pm 0.1$. Other DNS by Gotoh (1998), Schorghofer (2000), Lindborg & Alvelius (2000), Lindborg & Vallgren (2010), and Chen et al. (2003) indicated that Equation 14 is recovered in the limit of very high Reynolds numbers by an extended direct-cascade inertial range using Newtonian viscosity and that $E(k) \sim k^{-3}$ is obtained by a variety of hyper- and hypoviscosity dissipations. The measured value of the Kolmogorov constant was $C' \simeq 1.3$, and the prediction (Equation 16) for $S_3^{(L)}(r)$ was verified with high accuracy.

The best setup for experimentally investigating the direct cascade is the flowing soap-film experiment because of the small thickness, which allows the development of very small scales. Moreover, the ratio $\alpha' = \alpha/\omega_{rms}$ is approximately 100 times smaller than for EML systems

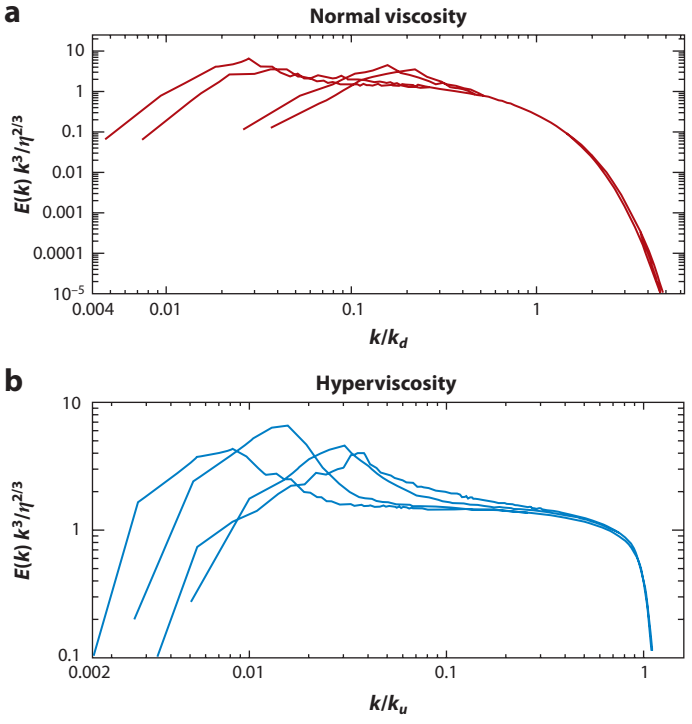

Figure 8

Compensated $E(k)$ for different resolution simulations with (*a*) normal viscosity for different size simulations from 512^2 to 4096^2 and (*b*) hyperviscosity for different size simulations from 512^2 to 2048^2 and for a forcing at higher k with 1024^2. Figure taken with permission from Borue (1993), copyright © 1993 by the American Physical Society.

because of the high levels of vorticity induced in the flowing soap film. The enstrophy cascade with a scaling exponent of approximately −3.3 was observed in three almost-identical versions of the soap-film experiment with different acquisition techniques (see **Figure 9**). Rutgers (1998) forced the film using two vertical combs. LDV was used to measure the velocity field at a high frequency in a small volume. Data taken in a spatial region of decaying turbulence showed a region of k^{-3} scaling in $E(k)$. In a second realization, Belmonte et al. (1999) used a horizontal comb to induce the turbulence, acquired velocity data using LDV, and observed an approximately k^{-3} spectrum over a range of scales (**Figure 9*a***). In a third experiment, Rivera et al. (1998) used 2D PIV to reconstruct the velocity and vorticity fields (**Figure 9*b***) as a function of the downstream distance. As discussed above, this approach eliminates the need for the Taylor hypothesis but has less precision owing to lower resolution: $E(k)$ for different downstream distances is shown in **Figure 9*c***. The experimental data of Rivera et al. (1998) show enstrophy flux with linear scaling of the mixed structure function, in agreement with Equation 17. Similar experiments by Rivera et al. (2003) used the filter approach to directly measure the PDF of enstrophy flux, showing its close agreement with DNS by Chen et al. (2003) and correlating coherent structures with the real-space structure of the enstrophy flux, consistent with the vortex-gradient-stretching picture of the direct cascade (see also Dubos & Babiano 2002).

The requirement of a constant enstrophy flux in the direct cascade led Kraichnan to propose a correction to the energy spectrum (see Section 2) of the form of Equation 14.

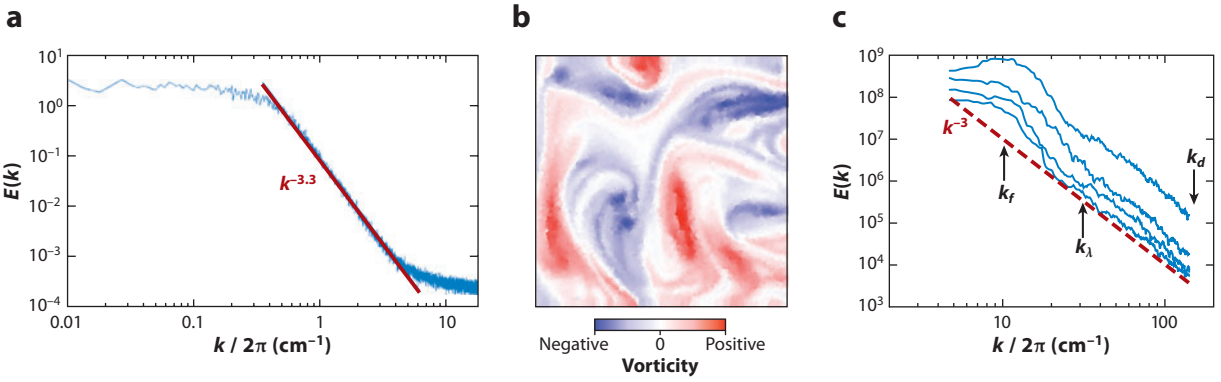

Figure 9

(*a*) $E(k)$ from laser-Doppler velocimetry in a flowing soap-film experiment by Belmonte et al. (1999). Figure reprinted with permission, copyright © 1999, American Institute of Physics. (*b*) Vorticity field from a similar experiment using particle image velocimetry/particle tracking velocimetry with (*c*) corresponding $E(k)$ at several distances downstream of the injection grid showing the overall decay of total energy, a scaling of $E(k) \sim k^{-3}$, and characteristic spatial scales: forcing scale (k_f), Taylor microscale (k_λ), and dissipation scale (k_d). Panels *b* and *c* obtained from the experimental system described in Rivera et al. (2003).

More recently, logarithmic corrections were predicted by Falkovich & Lebedev (1994) for higher-order correlators of the vorticity field in a form that is independent of the statistics of the forcing:

$$\langle [\omega(\mathbf{r})\omega(0)]^n \rangle \simeq \ln^{2n/3}(\ell_f/r). \tag{19}$$

The observation of these logarithmic corrections is a difficult task, as finite-size effects in simulations and experiments can be important. Many DNS (Benzi et al. 1986, Borue 1993, Lindborg & Alvelius 2000, Pasquero & Falkovich 2002, Chen et al. 2003, Lindborg & Vallgren 2010) and experiments (Rivera et al. 1998, 2003; Paret et al. 1999; Vorobieff et al. 1999) have presented results of power-law or logarithmic corrections/scalings in spectra and structure functions without definitive resolution. When considering logarithmic corrections, one needs to remember that the direct cascade is at the border of locality in the sense that dominant straining of small scales comes from the largest scales. Nonlocal effects can become dramatic if one considers a nonvanishing friction coefficient α in Equation 1. In this case, the enstrophy flux is no longer constant, and one expects power-law corrections, instead of logarithmic ones, to the energy spectrum.

Motivated by geophysical applications, Lilly (1972) generalized the Kraichnan argument described in Section 2 by including a friction term and recognized that this term removes all the enstrophy if viscosity is sufficiently small for a given α. Therefore, no strictly inertial range exists, and $E(k)$ is predicted to become steeper than -3 with a correction proportional to the friction coefficient α. Bernard (2000) and Nam et al. (2000) helped quantify this effect. Nam et al. (2000) assumed that because the enstrophy flux asymptotically vanishes, small-scale velocity fluctuations are passively transported by a smooth flow. Using results for the statistics of a passive scalar of Chertkov (1998) and Nam et al. (1999), they predicted a steepening of the spectrum (consistent, a posteriori, with the assumption of passive transport). The correction in the spectral exponent is proportional to the friction coefficient and depends on the distribution of finite-time Lyapunov exponents. The correction with respect to the dimensional prediction is different for different orders of vorticity structure functions $S_n^\omega(r) \equiv \langle [\delta\omega(r)]^n \rangle$ (Bernard 2000, Nam et al. 2000), and the direct cascade with friction becomes intermittent, i.e., $S_n^\omega(r) \sim r^{\zeta_n^\omega}$ with a nonlinear set of exponents ζ_n^ω predicted in terms of the distribution of the Lyapunov exponent.

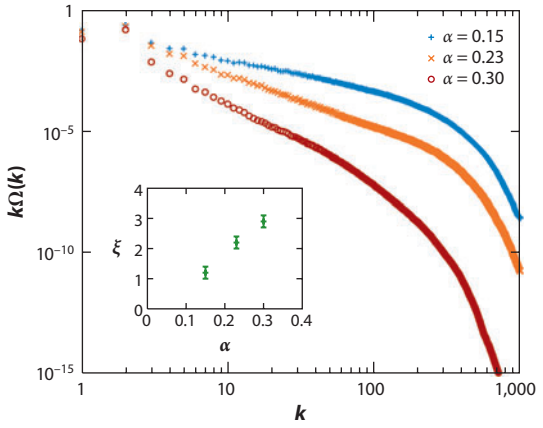

Figure 10

The vorticity spectrum $\Omega(k) = k^2 E(k)$ compensated with the classical prediction k^{-1} for different values of the friction coefficient: $\alpha = 0.15$ (*plus signs*), 0.23 (*crosses*), and 0.30 (*circled dots*). (*Inset*) The magnitude of the correction $k^{-1-\xi}$ as a function of α. Results from direct numerical simulations are from Boffetta et al. (2002), copyright © 2002 by the American Physical Society.

This issue was investigated numerically by Boffetta et al. (2002), who confirmed the previous findings and gave a physical argument, based on the statistics of Lagrangian trajectories, in support of the equivalence of the statistics of passive scalar and active vorticity. **Figure 10** shows the vorticity spectrum $\Omega(k) = k^2 E(k)$ obtained from DNS of Equation 1 for different values of α. The steepening with respect to the Batchelor-Kraichnan prediction $\Omega(k) \sim k^{-1}$ with increasing α is evident. The steepening of the spectrum by friction was also observed in EML experiments by Boffetta et al. (2005), despite the difficulty in realizing the direct cascade in EML experiments.

4.4. Double Cascade

The observation of coexisting direct and inverse cascades is a challenging task for both experiments and DNS. Per the discussion in Section 2, one needs both $\ell_\alpha \gg \ell_f$ and $\ell_f \gg \ell_\nu$ to observe well-developed inertial ranges. As a consequence, the ratio between the largest and smallest scale in the flow, ℓ_α/ℓ_ν, is required to be much larger than what is needed in 3D turbulence. Two experimental studies by Rutgers (1998) and Bruneau & Kellay (2005), both based on soap films, explored a novel approach to the study of the double cascade. In both cases, the flowing soap film was continuously forced by vertical arrays of cylinders. Velocity measurements, made with LDV, reveal that some energy moves to scales larger than the injection scale, that $E(k) \sim k^{-5/3}$ over a narrow range, and that energy flux is apparently to large scales. Conversely, this configuration yields velocity fields that are very heterogeneous owing to a complex combination of natural coarsening and lateral forcing, leaving doubt as to whether this is a good experimental realization of the double cascade despite the apparent spectral correspondence.

DNS by Boffetta (2007) and Boffetta & Musacchio (2010) showed the development of the double-cascade scenario by varying the resolution from $2{,}048^2$ to $32{,}768^2$ to test the convergence of the results at large Reynolds numbers. At the largest resolution, the extension of both the direct and inverse cascades is approximately two decades, as shown in **Figure 11*a***. Corresponding energy and enstrophy fluxes for the different runs are shown in **Figure 11*b*,*c***. Constant fluxes are observed over approximately one decade in both directions, with approximately 98% of the energy injected

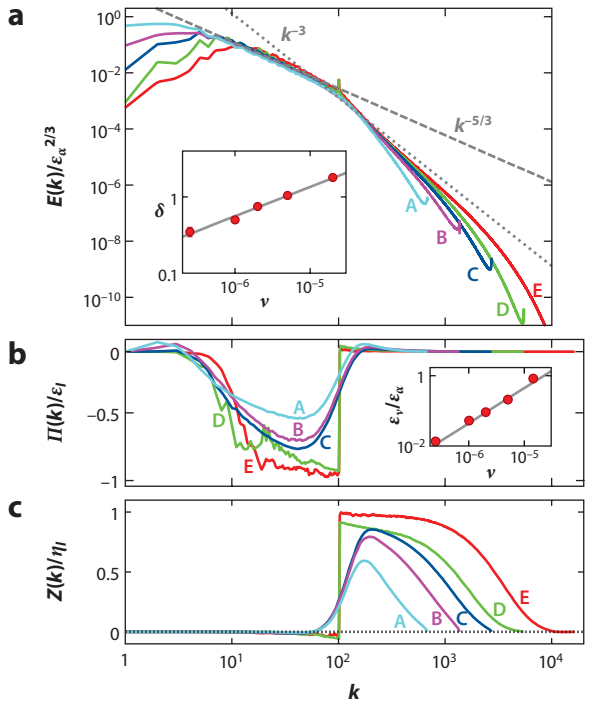

Figure 11

(*a*) $E(k)$ for different resolutions: (*A*) 2,048, (*B*) 4,096, (*C*) 8,192, (*D*) 16,384, and (*E*) 32,768. Dashed and dotted lines are the predictions $k^{-5/3}$ and k^{-3}, respectively. The inset shows the correction δ to the exponents -3 as a function of viscosity. (*b*) Energy and (*c*) enstrophy fluxes in Fourier space for simulations of the double cascade. The injection scale is $k_f = 100$. The inset in panel *b* shows the ratio of the viscous dissipation over large-scale friction dissipation. Figure adapted from Boffetta & Musacchio (2010), copyright © 2010 by the American Physical Society.

CONFORMAL INVARIANCE

An interesting property of 2D turbulence discovered recently is that of conformal invariance in the inverse cascade. Conformal invariance extends the property of scale invariance to the larger class of local transformations that preserve angles. In two dimensions, the high degree of symmetry imposed by the local transformations allows substantial analytical progress. As it is a property shared by several systems in 2D statistical mechanics, conformal invariance has been used to classify universality classes in critical phenomena. Using high-resolution DNS, Bernard et al. (2006) showed that vorticity isolines in the inverse cascade display conformal invariance and that vorticity clusters are remarkably close to that of critical percolation, one of the simplest universality classes of critical phenomena. This property has been extended to other 2D turbulent systems of physical and geophysical interest, suggesting that conformal invariance could be the rule in nonintermittent inverse cascades. These results represent a key step in the development of a statistical theory of inverse cascades in 2D fluids.

flowing to large scales (inset of **Figure 11*b***) and approximately 98% of the enstrophy going to small scales, in agreement with the discussion in Section 2. Finite Reynolds effects are evident for the direct cascade in which one observes a significant departure from the Kraichnan prediction. Nevertheless, there is strong evidence that the correction to the exponent is a finite-size effect that will disappear as viscosity is reduced. On the basis of these numerical simulations at high resolution, Bernard et al. (2006) were able to observe the property of conformal invariance for vorticity isolines in the inverse cascade (see the sidebar, Conformal Invariance).

SUMMARY POINTS

1. The existence and robustness of the inverse energy cascade with its Gaussian, nonintermittent statistics and solid $k^{-5/3}$ scaling with a Kolmogorov constant near 7 are well established.
2. The physical mechanism of the inverse cascade does not arise from vortex merger, but instead arises from the interaction of strain and vortices of different sizes, although an intuitive picture of this mechanism has not been realized.
3. The condensate state arising from the lack of dissipation at large scales results in the formation of large-scale vortices and a steepening of the low-k spectrum to approximately k^{-3}. Nevertheless, a decomposition that removes the dominant contribution of the large vortices reveals a less steep slope and a continued inverse energy cascade.
4. The direct cascade is understood as the large-scale straining of small-scale vortices through vortex-gradient stretching. Experiments for soap films and DNS show $E(k) \approx k^{-3}$ with slightly steeper slopes arising from frictional effects, whereas experiments in EML layers are significantly steeper, implying smoother flow and/or 3D effects.
5. The dual-cascade picture of forced Kraichnan-Batchelor turbulence finds solid support from DNS and, more tentatively, from experiments. We consider this classical picture as established and without major uncertainty provided that large-scale friction and small-scale viscosity are present to dissipate energy and enstrophy, respectively.

FUTURE ISSUES

1. A challenge for experiments is to measure directly the locality of the 2D inverse cascade, which is predicted to be less local than in three dimensions.
2. A better understanding of the effects of the condensate in 2D turbulence is important for applications of the theory in geophysical flows, which are often dominated by large vortices.
3. Evidence for or against logarithmic corrections or scalings is not definitive and is unlikely to be resolved in the near future owing to the difficulties differentiating frictional effects and insensitive logarithmic scaling.
4. The extension of the 2D turbulence picture to the more complex but still idealized model of geostrophic turbulence and especially to atmospheres and oceans remains a daunting challenge. In particular, the forcing scales in the atmosphere and oceans do not seem narrowly confined as in the idealized 2D turbulence problem, and the emergence of large-scale vortices reminiscent of the condensate problem complicates matters.

5. The extension of conformal invariance from the geometry of vorticity isolines to the statistics of turbulent fields would allow one to make analytical predictions on the correlation functions in the inverse cascade of 2D turbulence.

DISCLOSURE STATEMENT

The authors are not aware of any biases that might be perceived as affecting the objectivity of this review.

ACKNOWLEDGMENTS

We would like to thank Michael Rivera, Gregory Eyink, Shiyi Chen, Antonio Celani, Gregory Falkovich, and Stefano Musacchio for fruitful collaborations and extensive discussion about 2D turbulence. The authors also thank Michael Rivera and Jost von Hardenberg for help with several of the figures. R. Ecke was supported by the National Nuclear Security Administration of the U.S. Department of Energy at Los Alamos National Laboratory under contract DE-AC52-06NA25396. G. Boffetta acknowledges support from the Fulbright Foundation for a visit to the Center for Nonlinear Studies at Los Alamos National Laboratory where this review was begun.

LITERATURE CITED

Akkermans RAD, Kamp LPJ, Clercx HJH, van Heijst GJF. 2008. Intrinsic three-dimensionality in electromagnetically driven shallow flows. *Europhys. Lett.* 83:24001

Basdevant C, Legras B, Sadourny R, Béland M. 1981. A study of barotropic model flows: intermittency, waves and predictability. *J. Atmos. Sci.* 38:2305–26

Batchelor GK. 1959. Small-scale variation of convected quantities like temperature in turbulent fluid. Part 1. *J. Fluid Mech.* 5:113–33

Belmonte A, Goldburg WI, Kellay H, Rutgers MA, Martin B, Wu XL. 1999. Velocity fluctuations in a turbulent soap film: the third moment in two dimensions. *Phys. Fluids* 11:1196–200

Benzi R, Paladin G, Patarnello S, Santangelo P, Vulpiani A. 1986. Intermittency and coherent structures in two-dimensional turbulence. *J. Phys. A* 19:3771–84

Bernard D. 1999. Three-point velocity correlation functions in two-dimensional forced turbulence. *Phys. Rev. E* 60:6184–87

Bernard D. 2000. Influence of friction on the direct cascade of the 2D forced turbulence. *Europhys. Lett.* 50:333–39

Bernard D, Boffetta G, Celani A, Falkovich G. 2006. Conformal invariance in two-dimensional turbulence. *Nat. Phys.* 2:124–28

Boffetta G. 2007. Energy and enstrophy fluxes in the double cascade of two-dimensional turbulence. *J. Fluid Mech.* 589:253–60

Boffetta G, Celani A, Musacchio S, Vergassola M. 2002. Intermittency in two-dimensional Ekman-Navier-Stokes turbulence. *Phys. Rev. E* 66:026304

Boffetta G, Celani A, Vergassola M. 2000. Inverse energy cascade in two-dimensional turbulence: deviations from Gaussian behavior. *Phys. Rev. E* 61:R29–32

Boffetta G, Cenedese A, Espa S, Musacchio S. 2005. Effects of friction on 2D turbulence: an experimental study of the direct cascade. *Europhys. Lett.* 71:590–96

Boffetta G, Musacchio S. 2010. Evidence for the double cascade scenario in two-dimensional turbulence. *Phys. Rev. E* 82:016307

Boffetta G, Sokolov I. 2002. Statistics of two-particle dispersion in two-dimensional turbulence. *Phys. Fluids* 14:3224–32

Bondarenko N, Gak E, Gak M. 2002. Application of MHD effects in electrolytes for modeling vortex processes in natural phenomena and in solving engineering-physical problems. *J. Eng. Phys. Thermophys.* 75:1234–47

Borue V. 1993. Spectral exponents of enstrophy cascade in stationary two-dimensional homogeneous turbulence. *Phys. Rev. Lett.* 71:3967–70

Borue V. 1994. Inverse energy cascade in stationary two-dimensional homogeneous turbulence. *Phys. Rev. Lett.* 72:1475–78

Bos W, Bertoglio J. 2009. Large-scale bottleneck effect in two-dimensional turbulence. *J. Turbul.* 10:1–8

Bracco A, McWilliams J, Murante G, Provenzale A, Weiss J. 2000. Revisiting freely decaying two-dimensional turbulence at millennial resolution. *Phys. Fluids* 12:2931–41

Bruneau C, Kellay H. 2005. Experiments and direct numerical simulations of two-dimensional turbulence. *Phys. Rev. E* 71:046305

Cardoso O, Marteau D, Tabeling P. 1994. Quantitative experimental study of the free decay of quasi-two-dimensional turbulence. *Phys. Rev. E* 49:454–61

Charney J. 1971. Geostrophic turbulence. *J. Atmos. Sci.* 28:1087–95

Chen S, Ecke R, Eyink G, Rivera M, Wan M, Xiao Z. 2006. Physical mechanism of the two-dimensional inverse energy cascade. *Phys. Rev. Lett.* 96:084502

Chen S, Ecke R, Eyink G, Wang X, Xiao Z. 2003. Physical mechanism of the two-dimensional enstrophy cascade. *Phys. Rev. Lett.* 91:214501

Chertkov M. 1998. On how a joint interaction of two innocent partners (smooth advection and linear damping) produces a strong intermittency. *Phys. Fluids* 10:3017–19

Chertkov M, Connaughton C, Kolokolov I, Lebedev V. 2007. Dynamics of energy condensation in two-dimensional turbulence. *Phys. Rev. Lett.* 99:084501

Chomaz JM. 2001. The dynamics of a viscous soap film with soluble surfactant. *J. Fluid Mech.* 442:387–409

Couder Y, Chomaz J, Rabaud M. 1989. On the hydrodynamics of soap films. *Physica D* 37:384–405

Cummins PF, Holloway G. 2010. Reynolds stress and eddy viscosity in direct numerical simulations of sheared two-dimensional turbulence. *J. Fluid Mech.* 657:394–412

Danilov S, Gurarie D. 2001. Nonuniversal features of forced two-dimensional turbulence in the energy range. *Phys. Rev. E* 63:020203

Dolzhanskii FV, Krymov VA, Manin DY. 1992. An advanced experimental investigation of quasi-two-dimensional shear flow. *J. Fluid Mech.* 241:705–22

Dubos T, Babiano A. 2002. Two-dimensional cascades and mixing: a physical space approach. *J. Fluid Mech.* 467:81–100

Dubos T, Babiano A, Paret J, Tabeling P. 2001. Intermittency and coherent structures in the two-dimensional inverse energy cascade: comparing numerical and laboratory experiments. *Phys. Rev. E* 64:036302

Eyink GL. 1996. Exact results on stationary turbulence in 2D: consequences of vorticity conservation. *Physica D* 91:97–142

Eyink G. 2006. A turbulent constitutive law for the two-dimensional inverse energy cascade. *J. Fluid Mech.* 549:191–214

Falkovich G, Lebedev V. 1994. Nonlocal vorticity cascade in two dimensions. *Phys. Rev. E* 49:R1800–3

Fjortoft R. 1953. On the changes in the spectral distribution of the kinetic energy for two-dimensional, non-divergent flow. *Tellus* 5:225–30

Fornberg B. 1977. A numerical study of 2-D turbulence. *J. Comput. Phys.* 25:1–31

Frisch U. 1995. *Turbulence: The Legacy of AN Kolmogorov*. Cambridge, UK: Cambridge Univ. Press

Frisch U, Kurien S, Pandit R, Pauls W, Ray SS, et al. 2008. Hyperviscosity, Galerkin truncation, and bottlenecks in turbulence. *Phys. Rev. Lett.* 101:144501

Frisch U, Sulem PL. 1984. Numerical simulation of the inverse cascade in two-dimensional turbulence. *Phys. Fluids* 27:1921–23

Gharib M, Derango P. 1989. A liquid film (soap film) tunnel to study two-dimensional laminar and turbulent shear flows. *Physica D* 37:406–16

Gotoh T. 1998. Energy spectrum in the inertial and dissipation ranges of two-dimensional steady turbulence. *Phys. Rev. E* 57:2984–91

Herring J, McWilliams J. 1985. Comparison of direct numerical simulation of two-dimensional turbulence with two-point closure: the effects of intermittency. *J. Fluid Mech.* 153:229–42

Hossain M, Matthaeus W, Montgomery D. 1983. Long-time states of inverse cascades in the presence of a maximum length scale. *J. Plasma Phys.* 30:479–93
Jullien M, Paret J, Tabeling P. 1999. Richardson pair dispersion in two-dimensional turbulence. *Phys. Rev. Lett.* 82:2872–75
Kellay H, Goldburg WI. 2002. Two-dimensional turbulence: a review of some recent experiments. *Rep. Prog. Phys.* 65:845–94
Kellay H, Wu XL, Goldburg WI. 1995. Experiments with turbulent soap films. *Phys. Rev. Lett.* 74:3975–78
Kellay H, Wu XL, Goldburg WI. 1998. Vorticity measurements in turbulent soap films. *Phys. Rev. Lett.* 80:277–80
Kraichnan R. 1967. Inertial ranges in two-dimensional turbulence. *Phys. Fluids* 10:1417–23
Kraichnan R. 1971. Inertial-range transfer in two- and three-dimensional turbulence. *J. Fluid Mech.* 47:525–35
Kraichnan RH, Montgomery D. 1980. Two-dimensional turbulence. *Rep. Prog. Phys.* 43:547–619
Lamorgese A, Caughey D, Pope S. 2005. Direct numerical simulation of homogeneous turbulence with hyperviscosity. *Phys. Fluids* 17:015106
Legras B, Santangelo P, Benzi R. 1988. High-resolution numerical experiments for forced two-dimensional turbulence. *Europhys. Lett.* 5:37–42
Lilly D. 1969. Numerical simulation of two-dimensional turbulence. *Phys. Fluids* 12:II-240–49
Lilly D. 1972. Numerical simulation studies of two-dimensional turbulence: I. Models of statistically steady turbulence. *Geophys. Astrophys. Fluid Dyn.* 3:289–319
Lindborg E. 1999. Can the atmospheric kinetic energy spectrum be explained by two-dimensional turbulence? *J. Fluid Mech.* 388:259–88
Lindborg E, Alvelius K. 2000. The kinetic energy spectrum of the two-dimensional enstrophy turbulence cascade. *Phys. Fluids* 12:945–47
Lindborg E, Vallgren A. 2010. Testing Batchelor's similarity hypotheses for decaying two-dimensional turbulence. *Phys. Fluids* 22:091704
Maltrud M, Vallis G. 1991. Energy spectra and coherent structures in forced two-dimensional and β-plane turbulence. *J. Fluid Mech.* 228:321–42
Marteau D, Cardoso O, Tabeling P. 1995. Equilibrium states of two-dimensional turbulence: an experimental study. *Phys. Rev. E* 51:5124–27
McWilliams J. 1984. The emergence of isolated coherent vortices in turbulent flow. *J. Fluid Mech.* 146:21–43
Nam K, Antonsen TM, Guzdar PN, Ott E. 1999. *k* spectrum of finite lifetime passive scalars in Lagrangian chaotic fluid flows *Phys. Rev. Lett.* 83:3426–29
Nam K, Ott E, Antonsen TM, Guzdar PN. 2000. Lagrangian chaos and the effect of drag on the enstrophy cascade in two-dimensional turbulence. *Phys. Rev. Lett.* 84:5134–37
Novikov E. 1965. Functionals and the method of random forces in the theory of turbulence. *Sov. Phys. JETP* 20:1290–94
Paret J, Jullien M, Tabeling P. 1999. Vorticity statistics in the two-dimensional enstrophy cascade. *Phys. Rev. Lett.* 83:3418–21
Paret J, Marteau D, Paireau O, Tabeling P. 1997. Are flows electromagnetically forced in thin stratified layers two dimensional? *Phys. Fluids* 9:3102–4
Paret J, Tabeling P. 1997. Experimental observation of the two-dimensional inverse energy cascade. *Phys. Rev. Lett.* 79:4162–65
Paret J, Tabeling P. 1998. Intermittency in the two-dimensional inverse cascade of energy: experimental observations. *Phys. Fluids* 10:3126–36
Pasquero C, Falkovich G. 2002. Stationary spectrum of vorticity cascade in two-dimensional turbulence. *Phys. Rev. E* 65:056305
Rivera M, Vorobieff P, Ecke RE. 1998. Turbulence in flowing soap films: velocity, vorticity, and thickness fields. *Phys. Rev. Lett.* 81:1417–20
Rivera M, Wu XL. 2000. External dissipation in driven two-dimensional turbulence. *Phys. Rev. Lett.* 85:976–79
Rivera M, Wu XL. 2002. Homogeneity and the inertial range in driven two-dimensional turbulence. *Phys. Fluids* 14:3098–108
Rivera M, Wu XL, Yeung C. 2001. Universal distribution of centers and saddles in two-dimensional turbulence. *Phys. Rev. Lett.* 87:044501

Rivera MK, Daniel WB, Chen SY, Ecke RE. 2003. Energy and enstrophy transfer in decaying two-dimensional turbulence. *Phys. Rev. Lett.* 90:104502
Rivera MK, Ecke RE. 2005. Pair dispersion and doubling time statistics in two-dimensional turbulence. *Phys. Rev. Lett.* 95:194503
Rutgers MA. 1998. Forced 2D turbulence: experimental evidence of simultaneous inverse energy and forward enstrophy cascades. *Phys. Rev. Lett.* 81:2244–47
Salmon R. 1998. *Lectures on Geophysical Fluid Dynamics*. New York: Oxford Univ. Press
Schorghofer N. 2000. Energy spectra of steady two-dimensional turbulent flows. *Phys. Rev. E* 61:6572–77
Shats M, Byrne D, Xia H. 2010. Turbulence decay rate as a measure of flow dimensionality. *Phys. Rev. Lett.* 105:264501
Shats MG, Xia H, Punzmann H. 2005. Spectral condensation of turbulence in plasmas and fluids and its role in low-to-high phase transitions in toroidal plasma. *Phys. Rev. E* 71:046409
Siggia ED, Aref H. 1981. Point-vortex simulation of the inverse energy cascade in two-dimensional turbulence. *Phys. Fluids* 24:171–73
Smith L, Yakhot V. 1993. Bose condensation and small-scale structure generation in a random force driven 2D turbulence. *Phys. Rev. Lett.* 71:352–55
Smith L, Yakhot V. 1994. Finite-size effects in forced two-dimensional turbulence. *J. Fluid Mech.* 274:115–38
Sommeria J. 1986. Experimental study of the two-dimensional inverse energy cascade in a square box. *J. Fluid Mech.* 170:139–68
Tabeling P. 2002. Two-dimensional turbulence: a physicist approach. *Phys. Rep.* 362:1–62
Twardos MJ, Arratia PE, Rivera MK, Voth GA, Gollub JP, Ecke RE. 2008. Stretching fields and mixing near the transition to nonperiodic two-dimensional flow. *Phys. Rev. E* 77:056315
van Heijst G, Clercx H. 2009. Laboratory modeling of geophysical vortices. *Annu. Rev. Fluid Mech.* 41:143–64
Vorobieff P, Rivera M, Ecke RE. 1999. Soap film flows: statistics of two-dimensional turbulence. *Phys. Fluids* 11:2167–77
Voth GA, Saint TC, Dobler G, Gollub JP. 2003. Mixing rates and symmetry breaking in two-dimensional chaotic flow. *Phys. Fluids* 15:2560–66
Williams BS, Marteau D, Gollub JP. 1997. Mixing of a passive scalar in magnetically forced two-dimensional turbulence. *Phys. Fluids* 9:2061–80
Xia H, Byrne D, Falkovich G, Shats M. 2011. Upscale energy transfer in thick turbulent fluid layers. *Nat. Phys.* 7:321–24
Xia H, Punzmann H, Falkovich G, Shats MG. 2008. Turbulence-condensate interaction in two dimensions. *Phys. Rev. Lett.* 101:194504
Xiao Z, Wang X, Chen S, Eyink G. 2009. Physical mechanism of the inverse energy cascade of two-dimensional turbulence: a numerical investigation. *J. Fluid Mech.* 619:1–44
Yakhot V. 1999. Two-dimensional turbulence in the inverse cascade range. *Phys. Rev. E* 60:5544–51

Annual Review of
Fluid Mechanics

Volume 44, 2012

Contents

Indexes

Errata

An online log of corrections to *Annual Review of Fluid Mechanics* articles may be found at http://fluid.annualreviews.org/errata.shtml